Nanoscale

Molecular Simulations of Water Adsorption and Transport in Mesopores with Varying Hydrophilicity Arrangements

Journal:	*Nanoscale*
Manuscript ID	NR-ART-03-2018-002016.R1
Article Type:	Paper
Date Submitted by the Author:	11-May-2018
Complete List of Authors:	Kashiwagi, Kentaro; The University of Tokyo, Department of Mechanical Engineering Suh, Donguk; Keio University, Department of Mechanical Engineering Hwang, Junho; The University of Tokyo, Mechanical Engineering Hsu, Wei-Lun; University of Tokyo, Mechanical Engineering; University of Melbourne School of Ecosystem and Forest Sciences, Daiguji, Hirofumi; The University of Tokyo, Department of Mechanical Engineering

Molecular Simulations of Water Adsorption and Transport in Mesopores with Varying Hydrophilicity Arrangements

*Kentaro Kashiwagi‡, Donguk Suh‡, Junho Hwang, Wei-Lun Hsu, and Hirofumi Daiguji**

Department of Mechanical Engineering, The University of Tokyo, 7-3-1 Hongo, Bunkyo-ku, Tokyo 113-8656, Japan

KEYWORDS: Adsorption, Desorption, Capillary Condensation, Grand Canonical Monte Carlo, Grand Canonical Ensemble Molecular Dynamics

ABSTRACT

The adsorption and transport of water in an open cylindrical mesopore with two different inner surface arrangements of hydrophilicities were examined by molecular simulations. The first model has a weak hydrophilic surface at both entrances of the pore and a stronger hydrophilic surface in the mid-section. The second pore has the stronger hydrophilic surfaces at the entrances and the weaker in the middle region. The simulation results show that the water adsorption

isotherms obtained from Grand Canonical Monte Carlo simulations and pore filling curves acquired from Grand Canonical Molecular Dynamics simulations change depending on the arrangement of the strong and weak hydrophilic surfaces. In the first model, water condensation focuses on the mid-section forming a liquid bridge or film, which creates a concave meniscus accelerating subsequent adsorption within the pore. Two bridges form in the entrance regions, where a cavity naturally occurs in between the films, in the second model. The different filling and emptying mechanisms clearly change the adsorption-desorption characteristics for the two pore types, but the second type generally showed faster transitions overall. Flux and meniscus analysis also reveals a circulating flow at the menisci of the interfaces within the pore. The results are expected to be valuable in understanding the effects of interior surface modification of nanopores in future applications.

1. Introduction

Porous materials possessing effective adsorption-desorption characteristics due to high volumetric surface areas have demonstrated great promise in resolving challenges in a broad range of fields from the environment to medicine and beyond[1, 2]. Applications in the fields of dehumidification for desiccant air-conditioning systems[3-6], direct water harvesting from air[7-9], carbon dioxide capture[10], enhancement of dialysis components[11], catalytic systems[12-14], materials synthesis[15, 16], and protein loading for drug delivery[17, 18] have attracted growing attention due to the flexible liquid collecting and releasing abilities of these porous materials. In comparison with conventional absorbents consisting of a wide range of pore diameter distributions, the recent development of nanotechnology has achieved a synthesis of well-ordered and well-structured materials having unique characteristics of spontaneous adsorption and desorption within a

specific range of humidity accompanied by an outstanding storage capacity[19-23]. To improve the performance of these materials, a fundamental understanding of the physical mechanism of transport inside these porous materials needs clarification.

Due to the minuscule scale of confinement, experimental visualization of water transport processes into porous materials in real-time is challenging. Therefore, molecular simulations have been crucial in attaining new insight of the physics. Most of the early studies concerning nanopore transport were focused on understanding the adsorption-desorption hysteresis and dynamics through lattice gas models in slit pores[24-28]. Molecular simulations were also used to examine various pore configurations[29], in obtaining phase diagrams[30-33] and separating mixtures[34-38] for noble gases. Naturally, the confinement behavior of water became of great interest and numerous studies have been conducted on different pore sizes[39-42], various water phases[43-46], and ion or protein transport[47-50]. Using Grand Canonical Molecular Dynamics (GCMD)[51], Yamashita and Daiguji[52] investigated the mechanisms of water uptake in a silica nanopore. It was pointed out that the water molecules can either transport through the water film formed on the pore surface or water bridges in the nanopore. To elucidate the complete water adsorption-desorption processes in nanopores, an electrostatics-based coarse-grained model was employed to increase spatial and temporal calculation scales[53-57]. It was revealed that the initial adsorption rate increased exponentially with the increase in chemical potential. Furthermore, as soon as a water bridge connecting water molecules across the center of the nanopore was established, a rapid increase in the adsorption rate was observed.

Although previous molecular dynamics studies have provided significant insight into water behavior in nanopores, thus deepening our understanding in the formation of capillary condensation and evaporation processes, the effect of varying pore surface characteristics on the

formation of capillary condensation and evaporation processes has not yet been clarified. Regarding water imbibition in nanopores, Stukan et al.[58] theoretically investigated nanopores with various physical and chemical attributes. It was shown that the reduction in the meniscus velocity due to an increase in roughness and capillary wettability can be significant. Similar effects could be observed in water vapor adsorption in nanopores and the capillary condensation and evaporation processes could be altered by modifying the inner surfaces of the pore.

The objective of this research is to clarify the influence of how the difference in hydrophilicity within a pore surface can affect the adsorption-desorption characteristics of water by molecular simulations. General materials of interest do not have uniform pore sizes or uniform pore surfaces. Normally, water bridges are formed from nonuniform sites within the pore, and it is thought that each water bridge grows or coalesces. In this research, we investigate two models which have different hydrophilicity arrangements on the pore surface. Before examining the transport properties, an investigation into the state of adsorption of water in the pore at the equilibrium state was conducted. Subsequently, a nonequilibrium molecular dynamics simulation was performed by keeping the gas phase at a constant temperature and pressure, thereby simulating realistic conditions.

2. Methodology

2.1. Pore Model and Simulation Setup

A cylindrical pore was prepared in three steps, where the first was simulating bulk liquid in a cuboid cell of 4.0 nm × 4.0 nm × 40.0 nm as shown in Fig. 1 (a). After equilibration, one snapshot was taken and the mid-section (4.0 nm × 4.0 nm × 20.0 nm) region was considered to be a solid block. A cylindrical pore with a diameter of 2.8 nm was made through the *z*-axis of

this block. As in Fig. 1 (b) the block was centered to the origin, and across the longitudinal axis, two different regions were classified: inner (-5 nm ≤ z ≤ 5 nm) and outer (-10 nm ≤ z ≤ -5 nm and 5 nm ≤ z ≤ 10 nm). In this study, two pore models are studied, where the first (Model 1) has a high hydrophilicity on the inner region and low hydrophilicity on the outer. The second (Model 2) pore is opposite of the former, where the low hydrophilicity is the inner region and stronger on the outer. The colors in Fig. 1(b) and (c) simply distinguish the two different regions. The final preparation step is to assign interaction parameters corresponding to high and low hydrophilicities.

Figures 1 (b) and (c) show the systems used for calculating the adsorption-desorption isotherms by the Grand Canonical Monte Carlo (GCMC) method, and the system used for calculating the adsorption-desorption processes by GCMD, respectively. In Fig. 1 (b), the constructed mesopore is placed at the center of a calculation cell that has dimensions of 4.0 nm × 4.0 nm × 40.0 nm. Four types of trials (translation, rotation, insertion, and removal) were run 2.0 $\times 10^4$ times for each step at the same probability. The translational and angular velocities were randomly assigned according to the Maxwell–Boltzmann distribution at 350 K.

Fig. 1 (c) presents the GCMD system, where the origin of the pore used for GCMC was aligned with that of the calculation cell of 4.0 nm × 4.0 nm × 5100.0 nm. Water vapor was initially equilibrated in the entire system including the pore region. Thereafter, the amount of water was controlled solely in the outer regions of the calculation cell (-2550 nm ≤ z ≤ -50 nm and 50 nm ≤ z ≤ 2550 nm) through GCMC for every 2000 time steps. Molecular dynamics was the default and general periodic boundary conditions were used in all directions. Besides the GCMC region, an interfacial region (-50 nm ≤ z ≤ -10 nm and 10 nm ≤ z ≤ 50 nm) was set, where the motion of water was governed by molecular dynamics as was in the pore region

throughout the whole simulation. An in-house code was developed to conduct this simulation, where further information on the setup and validity has been previously reported[56, 57].

The electrostatics-based (ELBA) coarse-grained model[53, 54] was used for all molecules. The ELBA model assumes the molecules to be monatomic, where the dipole moment residing at the center of the sphere, is calculated through a Stockmayer type potential function coupled with Lennard-Jones interactions[59]. The parameters of the water molecule are shown in Table 1. ELBA interactions were used between water and wall molecules, which can be found in Table 2. Different parameters were used for the high and low hydrophilic regions, where the former produces complete wetting on the surface and the latter creates around a 20° contact angle. The parameters used in this study were taken from pore 1 and pore 3 in Yamashita et al[57], which were determined by assuming the gas to be ideal and replicate water at 350 K and 41.94 kPa. In these conditions, saturated vapor molecule number was 695.9 for the fixed volume. Further details on how the parameters were determined and the setup can be found in references [56, 57].

2.2. Adsorption-Desorption Isotherm

The adsorption of water at different chemical potentials was calculated by GCMC. The system temperature was kept at 350 K. The GCMC simulation for this study consists of four trials: translation, rotation, insertion, and deletion. All trials were performed throughout the system (-20 nm $\leq z \leq$ 20 nm). The translational velocity and angular velocity of a molecule followed the Maxwell Boltzmann distribution at 350 K.

2.3. Adsorption Process Preparation

The chemical potential of the gas phase in Fig. 1(c) was kept constant, and adsorption of

water in the pore was calculated by GCMD. As previously stated, GCMC was implemented for every 2000 steps of MD calculations (Δt=5 fs) and the pore temperature was kept constant at 350 K by a Langevin thermal bath (time constant 0.5 ps^{-1}). To prepare the system before applying GCMD, 1800 and 1900 water molecules, for Models 1 and 2, respectively, were initially spread out inside the system and equilibrated for a constant particle number, volume, temperature for 20 ns. At this point, condensation will have occurred but a liquid bridge has yet to form. This is the onset point of capillary condensation in each adsorption isotherm, which will be further explained in the ensuing section. The chemical potentials for the gas phase regions are set to be the values just before the water bridged inside the pores, which were μ = -65.8 kJ mol^{-1} in Model 1 and μ = -65.0 kJ mol^{-1} in Model 2, thereafter the simulation was continued until the pore became fully saturated. Different adsorption processes were calculated by changing the chemical potential of the gas phase stepwise from μ_0 = -65.8 kJ mol^{-1} to μ_1 = -65.0, -64.8, -64.0, and -62.8 kJ mol^{-1} for Model 1 and from μ_0 = -65.0 kJ mol^{-1} to μ_1 = -64.3 and -62.8 kJ mol^{-1} in Model 2. These are the chemical potential values where significant events occur during the pore filling process.

2.4. Desorption Process Preparation

The desorption processes were calculated similarly as that of the adsorption process. The initial state was obtained again from a constant number, volume, temperature MD by scattering 4000 water molecules inside the pore and equilibrating for 20 ns at μ = -64.0 kJ mol^{-1} for Model 1 and μ = -65.1 kJ mol^{-1} for Model 2, which completely filled the pore. Subsequently, the desorption process was calculated by decreasing the chemical potential stepwise in the gas phase regions in Fig. 1 (c) from μ_0 = -64.0 kJ mol^{-1} to μ_1 = -68.0 and -70.0 kJ mol^{-1} for Model 1, and

from μ_0 = -65.1 kJ mol^{-1} to μ_1 = -68.0 and -70.0 kJ mol^{-1} for Model 2. These are the chemical potential values where significant events occur during the evacuating process.

3. Results and Discussion

3.1. Adsorption-Desorption Isotherms

Figure 2 (a) shows the superposition of adsorption-desorption isotherms of Models 1 and 2. The horizontal axis shows the chemical potential μ, whereas the vertical axis represents the number of water molecules residing in the pores (-10 nm $\leq z \leq$ 10 nm).

In Model 1, as μ increases as in panel (b), water first adsorbs onto the inner highly hydrophilic region and a water bridge (or plug) forms. An increasing μ increases the meniscus angle of contact, and the thickening bridge advances into the outer weak hydrophilic region. Finally, the entire pore is saturated with water. The adsorption-desorption isotherm for Model 1 shows a hysteresis (around μ = -66.0 kJ mol^{-1}), which is consistent with cylindrical pore types[60]. This type of hysteresis occurs because of the initial bridging and subsequent difference in the meniscus contact angle that manifests itself during adsorption and desorption.

On the other hand, as μ increases for Model 2 as in panel (c), water first adsorbs on the outer strong hydrophilic regions, and two water bridges are constructed consequently creating a cavity in the weak hydrophilic region. As condensation continues, the void in the middle weak hydrophilic region eventually gets fully packed with water. Unlike Model 1, though the pore is cylindrical, the adsorption-desorption isotherm shows an ink-bottle type hysteresis[29, 60], which centers around μ = -65.0 kJ mol^{-1}. The formation of the bridges at the inlets of the pore keeps water from freely entering the pore through ballistic gas transport and the inner menisci that are

the boundaries of the void prolong the basic shape, so a greater chemical potential is required for capillary condensation to occur for Model 2. Desorption basically occurs in the reverse order of adsorption at different μ values for both models. The fundamental mechanism of adsorption and desorption are consistent with Sarkisov and Monson[29], which examined an actual ink-bottle configuration.

The existence of a hysteresis is natural due to the menisci, where a concave meniscus will try to gather or keep water as much as possible. Therefore, a greater free energy difference is required to detach water from its denser interface than to attract it from a dilute ambient. Moreover, the concave nature of the meniscus itself is natural since the water-wall interaction is stronger than the water-water interaction, which is clear for the different contact angles in Fig. 2 (b) μ = -65.7 and μ = -64.0 kJ mol^{-1}.

Additionally, Model 2 has more adsorbed water than Model 1 even though the two have identical dimensions. The main reason for this discrepancy in the adsorbed amount is because of the difference in the pore boundaries with the gas. As previously state, the weaker hydrophilic region borders the vapor source in Model 1 and the stronger region borders that for Model 2. Therefore, the water in the outer region in Model 2 is more tightly packed and adjacent to an unlimited source, so more compression can be applied towards the inner region. In figurative terms, the water in Model 1 is being pulled inside as opposed to the pushing effect its counterpart exerts.

It is interesting to note that the discrepancy in the adsorption mechanism for both models not only exists during the capillary condensation process but moreover actually starts from the lowest chemical potential region. Model 2 initially has slightly more water inside the pore. This

is caused by the outer layer being more hydrophilic, so water entering the pore can easily attach to the outer region within the mesopore compared to Model 1. Furthermore, the chemical potential gradient between the vapor and the inner pore is the largest at the higher hydrophilic regions within the pore. The formation of a bridge produces menisci with smaller contact angles (larger meniscus curvature), which accelerates pore filling or evacuation. Therefore, capillary condensation is most favorable at the center of the pore in Model 1 because a broader area of the pore is filled with undulating water layers condensed within the pore that eventually merge to form a bridge. Note that the chemical potential between condensed layers within the pore and the bridge is very narrow as evidenced by the jump in Fig. 2a. Similarly, the outer regions in Model 2 produce menisci with smaller contact angles since it is more hydrophilic and the negative chemical potential gradient will accelerate capillary evaporation compared with Model 1. In contrast with Model 1, water in the inner region in Model 2 has a weaker affinity to the pore, so they transfer more easily towards the pore entrances.

Based on the results of the two different models, the arrangement of the hydrophilic surfaces clearly changes the location and number of bridging. A concave meniscus forming in the middle region as in Model 1 accelerates water filling as seen in Fig. 2, where the first jump in the amount of adsorbed water occurs at a lower μ compared with Model 2. The second jump in the isotherm for Model 2, which is not visible for Model 1, takes place when the void collapses. The two different hysteresis types observed in the adsorption isotherms suggests a qualitative effect of the arrangement of the strong and weak hydrophilic regions. This variation in the location and bridging during adsorption has also been reported by Monson[28] through mean field kinetic theory by simply lengthening the pore.

3.2. Adsorption Process

The filling rate plots in Fig. 3 show the number of water molecules that have adsorbed in the pore over time for Models 1 and 2. The curves show that the saturation time shortens as the initial chemical potential difference $\Delta\mu = \mu_1 - \mu_0$, which is the difference between the chemical potential of the gas phase μ_1 and the initial state μ_0, increases stepwise. The time when the water bridge is first formed is t_1 (circle), the time when the meniscus spans into the low hydrophilic region is noted as t_2 (triangle), and when the meniscus contact angle starts to change at the ends of the pore is t_3 (square). The exact times are summarized in Table 3.

Two linear fits were taken for times t_1 and t_2 each as the origins, where a solid line is for the former and dashed line for the latter. Monson[28] and Yamashita et al.[61] showed that the adsorption rate of water molecules increased once a bridge develops, and the slope of the linear fits increased, which is consistent with this study as seen in Fig. 3 (a). After a bridge initially forms in the stronger hydrophilic middle region, the growth of the bridge occurs axially by the advancement of the meniscus rather than radially (continuous condensation on the initially wetted layers). As the bridge continues to grow, the meniscus moves into the weaker hydrophilic region and the slope that originated from t_2 will decrease because there is relatively less water on the weaker hydrophilic surface. As $\Delta\mu$ increases, the chemical potential difference between the interior of the pore and the gas phase increases, so the wall at high $\Delta\mu$ readily has more water to sustain the growth of the water plug. Therefore, the slope difference before and after the bridge formation is more pronounced for lower $\Delta\mu$'s. In any case, the supply of water to the plugging in the low hydrophilic region is found to occur through the wetted layer on the surface rather than directly from the gas phase.

Figure 3 (b) presents the filling curves for Model 2. As in Model 1, the slopes of the linear fits for the filling curve changed with $\Delta\mu$. The time at which the first water bridge forms is t_{1-1}(circle) and the second is at t_{1-2} (second circle). The time when the menisci first comes into direct contact with the low hydrophilic region is represented by t_2 (triangle), and the point at which the meniscus contact angle transition occurs before full saturation of the pore is denoted as t_3 (square). A summary of the times is shown in Table 4. Similarly to Model 1, the curves were linearly fit with t_{1-1} and t_2 as their origins.

The flux of water vapor into and out of the pores at z = ±25 nm (Fig. 1(c)) for unit area and unit time are plotted in Fig. 4. This distance is 15 nm from the actual inlets of the pore, which was chosen to obtain better statistics. Panel (a) is for Model 1 at $\Delta\mu$= 3.0 kJ mol^{-1}, and panel (b) is Model 2 at $\Delta\mu$= 2.2 kJ mol^{-1}. The influx towards the pore (green line) is nearly constant since the source of the gas, which is kept at constant $\Delta\mu$, is located at the outskirts of the sliced regions, and therefore, a higher $\Delta\mu$ produces a greater influx. The outflux is water vapor coming back from the pore. The net flux calculated from the difference of in and out, reveals the detailed history of the bridge formation (circle), encroachment of the bridge to the weaker hydrophilic region (triangle), and the plug finally reaching the entrances of the pore (square). The events in the net flux are directly related to the changes in the filling rate slopes seen in Fig. 3. Through the flux evolution, one can find that the filling process in the pore is controlled by the amount of water vapor returning from the pore. As a bridge initially forms in the stronger hydrophilic region, water becomes more likely to stay in the pore rather than evaporate and return to the vapor region. After the plug moves into the weaker region, the effect of the decrease in the attachment strength can be clearly observed with the increase in the outflux. A final dip in the netflux once the edges of the meniscus meet the entrance can also be seen.

3.3. Desorption Process

Desorption initiates from the pore outlet, where the water in the pore is in contact with the dilute gas region that has a lower chemical potential. The desorption process for Model 1 is displayed in Fig. 5 (a) for different values of $\Delta\mu$. When the meniscus comes into contact with the different hydrophilic surface, the time is t_1, and when the bridge dissolves it is t_2. The time of the notable events are summarized in Table 5. The curves were linearly fit from the origins, which is the point when the pore is completely filled, and from t_1. From the slope decline, it can be seen that the desorption rate decreases after t_1. Before t_1, the desorption rate was greater because the water-wall interaction in the low hydrophilic region was relatively weak. Naturally, the desorption rate decreases because water tries to stay near the wall for the high hydrophilic region. Moreover, in Model 2 (Fig. 5b), the desorption curve changes with $\Delta\mu$, and has a different curvature as opposed to Model 1. Here, the time when the meniscus first crosses into the lower region is t_1, at the time when the film of water first disappears is t_{2-1}, followed by the next one at t_{2-2}. The times are summarized in Table 6. Smaller $\Delta\mu$'s for Model 2 compared to Model 1 were sufficient to trigger the phase transition as was the case for adsorption.

Model 2 initially shows similar desorption behavior with Model 1, but since the outer region has a stronger attraction with water, once a meniscus enters the weaker region, a bridge reappears again forming a cavity. This process is dissimilar to that found by GCMC in Fig. 2c, which is clear evidence that though GCMC has advantages such as less computational cost, the method has limitations in mimicking non-equilibrium processes. The reappearing cavity persists

during the entire desorption process until a bridge on either side dissolves. Note that unlike Model 1, the slope starting from the triangle is greater than that from the initial pore state.

Similarly to adsorption, the flux of water vapor in and out of the pores are in Fig. 6, where panel (a) is for Model 1 at $\Delta\mu$= 6.0 kJ mol^{-1} and panel (b) is Model 2 at $\Delta\mu$= 4.9 kJ mol^{-1}. The influx towards the pore is again nearly constant but lower than the case of adsorption. The net flux again shows the evolution of how the plugs become thinner, from when the meniscus first encounters the different surface (triangle) and to when the bridge eventually dissolves (circle). The events in the net flux directly correspond to the changes in the slopes seen in Fig. 5. The initial slope of the outer flow increases for Model 1 and decreases for Model 2 after the meniscus moves into the dissimilar hydrophilic region and gradually decreases after the bridge breaks apart because desorption must occur two-dimensionally. This is consistent with the different curvatures in both panels of Fig. 5 and the slope tendencies.

3.4. Flux Analysis

3.4.1 Adsorption

To better understand the dynamics of water molecules within the pore during adsorption and desorption, the flux was further analyzed for each model. As in Fig. 1 (c), the center of the pore is set as z = 0.0 nm and the entrances are located at z = ±10.0 nm. During the adsorption process, the radial distributions of the time-averaged flux at z = ±3.0, ±5.0, ±7.0, and ±9.0 nm are shown in Fig. 7. Note that the threshold between the strong and weak hydrophilic regions exist at z=±5.0 for both models. Spatial averages were taken in the radial direction right after the

meniscus has firmly established itself into the new region at t= 85 ns for Model 1 and t = 65 ns for Model 2, both for the largest $\Delta\mu$ values in each model. The sign of the flux was set to be in the same direction as that of the z-axis in Fig. 1 (c). At the observed time, the ascending axial centers of the bridges were located between z = ±7.0 nm and z = ± 9.0 nm as in the cross-section snapshot in panel (b), where one can see that flux J oscillates around zero for z = ±3.0 and ±5.0 nm. The small fluctuation is understandable since the regions are filled with bulk-like water. At the wall, the flux will become zero because no transport can happen beyond the wall surfaces. Additionally, at z = ±7.0 nm, a strong positive flux, which represents a strong current towards the entrances was seen with a negative flux near the pore walls. This means the center of the plug grows from water molecules that have condensed onto the pore surface descending from entrance regions of the walls and circulating into the plug core. The flow distribution at z = ± 9.0 nm clearly shows the flow direction of the condensed water layer heading towards the center.

In contrast, Model 2 is more complex since it has two bridges that encapsulate a void. The growth of the outer menisci at z=±7.0 nm follows that of Model 1, but as can be seen in Fig. 7 (c), the inner meniscus grows from the condensed vapor being transported into the inner region via the pore surfaces at z=±3.0 and ±5.0 nm. The circulating flow is the strongest at the boundary of the bridge and cavity interface of z = ±3.0 nm. Moreover, the overall transport is greater for model 2 than 1, which can be easily found from the summation of areas. Furthermore, a clear difference in the growth mechanism of the meniscus can be seen, where the meniscus will grow nearly uniformly across the radial direction for model 1, whereas, more attachment on the walls not only clearly precedes meniscus progression (advection), but also a contraction in the flux of the inner menisci is observable in the center region in model 2. This mechanism is clearly illustrated in Fig. 7 (d). Note that a clear Hagen-Pouiselle type flow can be observed at the outer

most region of z = ±9.0 nm for Model 2. In short, the controlling mechanism of Model 1 is adsorption, whereas Model 2 is a combination of adsorption and advection. This combination of adsorption and advection resembles the well-known *coffee-ring* effect[62].

3.4.2 Desorption

The spatial flux distribution for the desorption process of Model 1 in the axial directions at z = ±3.0, ±5.0, ±7.0, and ±9.0 nm for $\Delta\mu$ = 6.0 kJ mol^{-1} at t = 35 ns is summarized in Fig. 8 (a), which shows the interfaces of the contracting bridge residing in the stronger hydrophilic region. No flow can be seen near the core region of the pore at z = ±3 or ±5 nm, where the flux oscillation starts to increase closer to the wall. A clear positive to negative crossover occurs for z = ±7 nm, where the meniscus resides. From the analysis of the meniscus, one can gather that desorption occurs in the center of the meniscus rather than from the walls. Furthermore, a large positive flux occurs at the center as well as adjacent to the walls near the boundaries of the bridge (z = ±9 nm) in Model 1, which represents the adsorbed molecules exiting the pore by evaporation and through scaling the pore surface. A positive flux throughout the radial direction means molecules are emitted as vapor from the interface, which is intuitive since the hydrophilic interaction is weak near the walls. The combination of desorption through the interface and wall are identical pathways for adsorption. Panels (c) and (d) illustrate Model 2 under $\Delta\mu$ = 4.9 kJ mol^{-1} at t = 60 ns, where the flux distribution after the cavity develops. The former panel concerns the upper bridge and the latter explains the lower, respectively. The bridges are not symmetric as in Model 1 because of how the upper bridge formed after profuse depletion and regeneration of the bridge as shown in Fig. 5 (b). Panels (b) and (e) present the snapshots of the plug corresponding to the pore at the certain instances. After ample time has passed in Fig. 8 (c), the desorption pathways resemble that of adsorption with opposite sign, where a circulating

tendency occurred from the wall towards the radial center of the pore. Zero flux is seen at z = 3 nm except at the walls, which is where the molecules solely reside and move towards the pore exit. At the threshold of hydrophilicity (z = 5 nm), an inward flux is observable, whereas a strong outward flux occurs near the walls. The gradient of the flux levels out radially and only outward flux is observed near the exit (z = 9 nm). The crossover gradient in Fig. 8 (d) is similar for all axial positions except for that closest to the exit (z = -9 nm), where desorption occurs radially across its entirety. One can clearly observe desorption taking place from the walls.

3.5. Meniscus Analysis

In the previous section, the axial growth of the bridge into a plug was examined by flux analysis. Model 1 grew through condensing layers within the pore, whereas clear advective transport across the walls and towards the axial center of the pore could be observed for the second model. Here, further analysis has been conducted on how the curvature of the meniscus affects growth.

3.5.1 Adsorption

During the adsorption process, the analyzed results on the averaged curvature difference of all the menisci on both sides of the bridges regarding Model 2 were plotted in Fig. 9 for all $\Delta\mu$ conditions presented in Fig. 3 (b) at N = 2500 (t = 22.0 ns in $\Delta\mu$ = 2.2 kJ mol^{-1} and t = 70.0 ns in $\Delta\mu$ = 0.7 kJ mol^{-1}). The meniscus was calculated by spatially averaging the water density over a time range of $t - 0.5 \sim t + 0.5$ ns. The liquid-vapor interface was defined as the mean between the bulk liquid and bulk vapor densities of water. Panel (a) shows the menisci curvature differentials $\Delta\rho^{-1}$ of the upper and lower plugs forming the void and the corresponding instantaneous adsorption rates, which coincide with the slopes in Fig. 3(b). A summarized diagram of the menisci forming for all $\Delta\mu$ conditions is in panel (b). The subscripts U, L, O, and

I are Upper, Lower, Outer, and Inner corresponding to the placements of the menisci. Panel (b) shows the evolution of the center of the meniscus for different chemical potential conditions.

The radius of curvature contacting the outer gas phase is clearly larger than that constituting the void in Fig. 9 (b). Therefore, $\Delta\rho^{-1}$ for the inside is larger than that for the outside, which means there is more force acting towards the inside of the void. The evolution of the menisci center again shows that once the bridges form in the center of the highly hydrophilic regions, their initial positions are stable, which means that they are pinned. When the curvature gradient from inside and outside was small ($\rho_{U\text{-}O} - \rho_{U\text{-}I} = 0.03$ nm), the formation of the bridge stalled as can be seen from the bridge on the upper side in $\Delta\mu = 0.7$ kJ mol^{-1}. Furthermore, though the pore filling mechanism for Model 1 was based on vapor trapping in the menisci, the outer menisci in Model 2 are nearly stagnant and only the insides converge to the pore center. Therefore, it is clear that Model 1 is based purely on adsorption, whereas Model 2 is a combination of adsorption and advection from the outer menisci to the inner regions of the pore. The fact that the outer menisci have smaller curvatures (larger radius of curvature) and are closer to the source of condensation, entails the overall adsorption rate to be faster.

3.5.2 Desorption

Similarly, for desorption, all $\Delta\mu$ conditions in Fig. 5 (b) at $N = 3000$ ($t = 72.8$ ns in $\Delta\mu = 2.9$ kJ mol^{-1} and $t = 105.0$ ns in $\Delta\mu = 4.9$ kJ mol^{-1}) are plotted in Fig. 10. Panels (a) and (b) show how the increase in the chemical potential difference affects the curvature difference, which corresponds to the slope increase of the relaxation curve in Fig. 5 (b). The outer menisci have smaller radii, which produces a driving force outwards and the finite nature of the pore generates a natural pinning effect for the plugs. For both $\Delta\mu$ conditions, the meniscus of a single plug

initially contracted, but as the upper meniscus crossed into the weaker hydrophilic region a new bridge in the upper region formed shortly thereafter. Due to a void formation, the outer meniscus of the lower plug was pushed closer to the lower outlet. After the two bridges and the void was established, the lower one first dissolved for $\Delta\mu$=4.9 kJ mol^{-1}, whereas the upper vanished first for $\Delta\mu$ =2.9 kJ mol^{-1}. The centers of the plugs were pinned as seen in adsorption. The complex dynamics of the desorption process was nonobservable through GCMC calculations as previously stated. Further analysis of the intricacies of desorption will be dealt in further detail in a separate study.

4. Conclusion

The adsorption and desorption characteristics of water in an open cylindrical mesopore with two different inner surface arrangements of hydrophilicities were examined by molecular simulations. The simulation results showed that the water adsorption isotherms obtained from GCMC and pore filling curves acquired from GCMD change depending on the arrangement of the strong and weak hydrophilic surfaces. In Model 1, one liquid bridge forms in the mid-section of the pore, where the eventual creation of concave menisci accelerates subsequent adsorption within the pore. For Model 2, two bridges form at the entrance regions, and a cavity naturally occurs in between the two bridges. The difference in the saturating and evacuating mechanisms clearly change the adsorption-desorption characteristics for the two pore types, but Model 2 provided faster plugging in general because the source of the vapor was closer to the entrances, where the bridges develop.

The overall mechanism of pore filling for systems that have different hydrophilicity arrangements originates from pinning, where it is the preferential pinning of the vapor molecules onto the strong hydrophilic surface that builds the bridge, which forms menisci that expedite the capture of vapor. The initial condensation of the pore is key to further pore filling. Based on flux analysis, depending on the existence of a void, two distinct growth mechanisms occur. Model 1 showed that the condensed water would trail the pore walls towards the bridge, whereas, in Model 2, the water condensed on the outer menisci will rapidly transfer towards the void region at a faster rate through advection. A meniscus with a smaller radius of curvature forms on the interfaces of the void due to the flow traveling along the walls increasing the condensed layer thickness. The fact that the outer menisci have a larger radius and are closer to the source of condensation makes adsorption faster, which can suggest that when multiple liquid bridges can be made inside a pore, it will accelerate the filling process. The results are expected to be valuable in understanding the effects of interior surface modification to induce cavities in pores to enhance filling and evacuating for future applications.

AUTHOR INFORMATION

Corresponding Author

*Hirofumi Daiguji

Professor of Department of Mechanical Engineering, The University of Tokyo

Email: daiguji@thml.t.u-tokyo.ac.jp,

Tel: +81 3 5841 6971,

Fax: +81 3 5841 6971

Author Contributions

The manuscript was written through contributions of all authors. All authors have given approval to the final version of the manuscript. ‡These authors contributed equally.

Funding Sources

JST CREST program "Phase Interface Science for Highly Efficient Energy Utilization" and JST CREST Grant Number JPMJCR17I3, Japan.

Notes

The authors declare no competing financial interest.

ACKNOWLEDGMENT

This work was supported in part by JSPS Postdoctoral Fellowship Grant Number P17068 for DS, JST CREST program "Phase Interface Science for Highly Efficient Energy Utilization," and JST CREST Grant Number JPMJCR17I3, Japan for HD.

REFERENCES

1. M. E. Davis, *Nature*, 2002, **417**, 813-821.
2. S. Kataoka, Y. Takeuchi, A. Kawai, M. Yamada, Y. Kamimura and A. Endo, *Langmuir*, 2013, **29**, 13562-13567.
3. A. Zouaoui, L. Zili-Ghedira and S. Ben Nasrallah, *Int. J. Heat Technol.*, 2016, **34**, 103-109.
4. A. Kumar and A. Yadav, *Int. J. Refrig.-Rev. Int. Froid*, 2016, **69**, 51-63.
5. Y. Jiang, T. S. Ge, R. Z. Wang and L. M. Hu, *Int. J. Refrig.-Rev. Int. Froid*, 2015, **51**, 169-179.
6. K. Nawaz, S. J. Schmidt and A. M. Jacobi, *International Journal of Heat and Mass Transfer*, 2014, **74**, 25-34.

7. S. Baker, T. Volova, S. V. Prudnikova, S. Satish and M. N. N. Prasad, *Environ. Toxicol. Pharmacol.*, 2017, **53**, 10-17.
8. H. Yanagihara, K. Yamashita, A. Endo and H. Daiguji, *The Journal of Physical Chemistry C*, 2013, **117**, 21795-21802.
9. A. Endo, T. Yamaura, K. Yamashita, F. Matsuoka, E. Hihara and H. Daiguji, *Journal of Colloid and Interface Science*, 2012, **367**, 409-414.
10. M. B. Sweatman and N. Quirke, *Langmuir*, 2001, **17**, 5011-5020.
11. M. Aoyama, T. Mizuno, E. Tatsumi, Y. Taenaka, Y. Nemoto, Y. Okamoto, Y. Takemoto, T. Naganuma and T. Nakatani, *Artif. Organs*, 2009, **33**, 1127-1132.
12. H. Zou, R. Wang, J. Dai, Y. Wang, X. Wang, Z. Zhang and S. Qiu, *Chemical Communications*, 2015, **51**, 14601-14604.
13. S. Li, X. Jiao and H. Yang, *Langmuir*, 2013, **29**, 1228-1237.
14. H. Yang, X. Jiao and S. Li, *Chemical Communications*, 2012, **48**, 11217-11219.
15. C. Ma, H. Wu, Z. H. Huang, R. H. Guo, M. B. Hu, C. Kübel, L. T. Yan and W. Wang, *Angew. Chem. Int. Ed.*, 2015, **54**, 15699-15704.
16. Z. Huang, P. Chen, Y. Yang and L.-T. Yan, *The Journal of Physical Chemistry Letters*, 2016, **7**, 1966-1971.
17. X. Du, C. X. Zhao, H. W. Huang, Y. Q. Wen and X. J. Zhang, *Progress in Chemistry*, 2016, **28**, 1131-1147.
18. S. H. Shen, Y. S. Wu, Y. C. Liu and D. C. Wu, *International Journal of Nanomedicine*, 2017, **12**, 4085-4109.
19. S. Inagaki, Y. Fukushima, K. Kuroda and K. Kuroda, *Journal of Colloid and Interface Science*, 1996, **180**, 623-624.
20. A. Shimojima, H. Kuge and K. Kuroda, *J. Sol-Gel Sci. Technol.*, 2010, **57**, 263-268.
21. T. Kimura, H. Tamura, M. Tezuka, D. Mochizuki, T. Shigeno, T. Ohsuna and K. Kuroda, *Journal of the American Chemical Society*, 2008, **130**, 201-209.
22. A. G. Slater and A. I. Cooper, *Science*, 2015, **348**.
23. J. Hwang, S. Kataoka, A. Endo and H. Daiguji, *The Journal of Physical Chemistry C*, 2015, **119**, 26171-26182.
24. U. M. B. Marconi and F. v. Swol, *EPL (Europhysics Letters)*, 1989, **8**, 531.
25. U. M. B. Marconi and F. Van Swol, *PhRvA*, 1989, **39**, 4109-4116.
26. L. Sarkisov and P. A. Monson, *Physical Review E*, 2002, **65**.
27. E. Kierlik, P. A. Monson, M. L. Rosinberg and G. Tarjus, *Journal of Physics-Condensed Matter*, 2002, **14**, 9295-9315.
28. P. A. Monson, *Journal of Chemical Physics*, 2008, **128**.
29. L. Sarkisov and P. A. Monson, *Langmuir*, 2001, **17**, 7600-7604.
30. B. K. Peterson and K. E. Gubbins, *Molecular Physics*, 1987, **62**, 215-226.
31. G. S. Heffelfinger, F. van Swol and K. E. Gubbins, *Molecular Physics*, 1987, **61**, 1381-1390.
32. M. Sliwinska-Bartkowiak, J. Gras, R. Sikorski, R. Radhakrishnan, L. Gelb and K. E. Gubbins, *Langmuir*, 1999, **15**, 6060-6069.
33. L. D. Gelb and K. E. Gubbins, *Molecular Physics*, 1999, **96**, 1795-1804.
34. G. S. Heffelfinger, Z. M. Tan, K. E. Gubbins, U. M. B. Marconi and F. van Swol, *Molecular Simulation*, 1989, **2**, 393-411.
35. G. S. Heffelfinger, Z. Tan, K. E. Gubbins, U. M. B. Marconi and F. van Swol, *International Journal of Thermophysics*, 1988, **9**, 1051-1060.

36. L. D. Gelb, K. E. Gubbins, R. Radhakrishnan and M. Sliwinska-Bartkowiak, *Rep. Prog. Phys.*, 1999, **62**, 1573-1659.
37. L. D. Gelb and K. E. Gubbins, *Physical Review E*, 1997, **56**, 3185-3196.
38. L. D. Gelb and K. E. Gubbins, *Physica A*, 1997, **244**, 112-123.
39. M. Rovere, M. A. Ricci, D. Vellati and F. Bruni, *Journal of Chemical Physics*, 1998, **108**, 9859-9867.
40. E. Spohr, C. Hartnig, P. Gallo and M. Rovere, *Journal of Molecular Liquids*, 1999, **80**, 165-178.
41. J. Puibasset and R. J. M. Pellenq, *Journal of Chemical Physics*, 2003, **118**, 5613-5622.
42. M. Rovere and P. Gallo, *Eur. Phys. J. E*, 2003, **12**, 77-81.
43. R. J. Mashl, S. Joseph, N. R. Aluru and E. Jakobsson, *Nano Letters*, 2003, **3**, 589-592.
44. K. Koga, X. C. Zeng and H. Tanaka, *Chemical Physics Letters*, 1998, **285**, 278-283.
45. K. Koga, X. C. Zeng and H. Tanaka, *Physical Review Letters*, 1997, **79**, 5262-5265.
46. J. C. Liu, P. A. Monson and F. van Swol, *Journal of Physical Chemistry C*, 2007, **111**, 15976-15981.
47. G. Hummer, *Molecular Physics*, 2007, **105**, 201-207.
48. P. Demontis, G. Stara and G. B. Suffritti, *Microporous Mesoporous Mat.*, 2005, **86**, 166-175.
49. C. Corsaro, V. Crupi, F. Longo, D. Majolino, V. Venuti and U. Wanderlingh, *Physical Review E*, 2005, **72**.
50. J. C. Rasaiah, S. Garde and G. Hummer, *Annu. Rev. Phys. Chem.*, 2008, **59**, 713-740.
51. L. Sarkisov and P. A. Monson, *Langmuir*, 2000, **16**, 9857-9860.
52. K. Yamashita and H. Daiguji, *The Journal of Physical Chemistry C*, 2015, **119**, 3012-3023.
53. M. Orsi and J. W. Essex, *PLoS ONE*, 2011, **6**, e28637.
54. M. Orsi, *Molecular Physics*, 2013, **112**, 1566-1576.
55. W. Ding, M. Palaiokostas and M. Orsi, *Molecular Simulation*, 2015, **42**, 337-346.
56. K. Yamashita, K. Kashiwagi, A. Agrawal and H. Daiguji, *Molecular Physics*, 2017, **115**, 328-342.
57. K. Yamashita and H. Daiguji, *Molecular Physics*, 2016, **114**, 884-894.
58. M. R. Stukan, P. Ligneul and E. S. Boek, *Oil Gas Sci. Technol.*, 2012, **67**, 737-742.
59. W. H. Stockmayer, *The Journal of Chemical Physics*, 1941, **9**, 398-402.
60. K. S. W. Sing, D. H. Everett, R. A. W. Haul, L. Moscou, R. A. Pierotti, J. Rouquerol and T. Siemieniewska, in *Handbook of Heterogeneous Catalysis*, Wiley-VCH Verlag GmbH & Co. KGaA, 2008, DOI: 10.1002/9783527610044.hetcat0065.
61. K. Yamashita, A. Endo and H. Daiguji, *The Journal of Physical Chemistry C*, 2013, **117**, 2096-2105.
62. J. J. Diao and M. G. Xia, *Colloids Surf. Physicochem. Eng. Aspects*, 2009, **338**, 167-170.

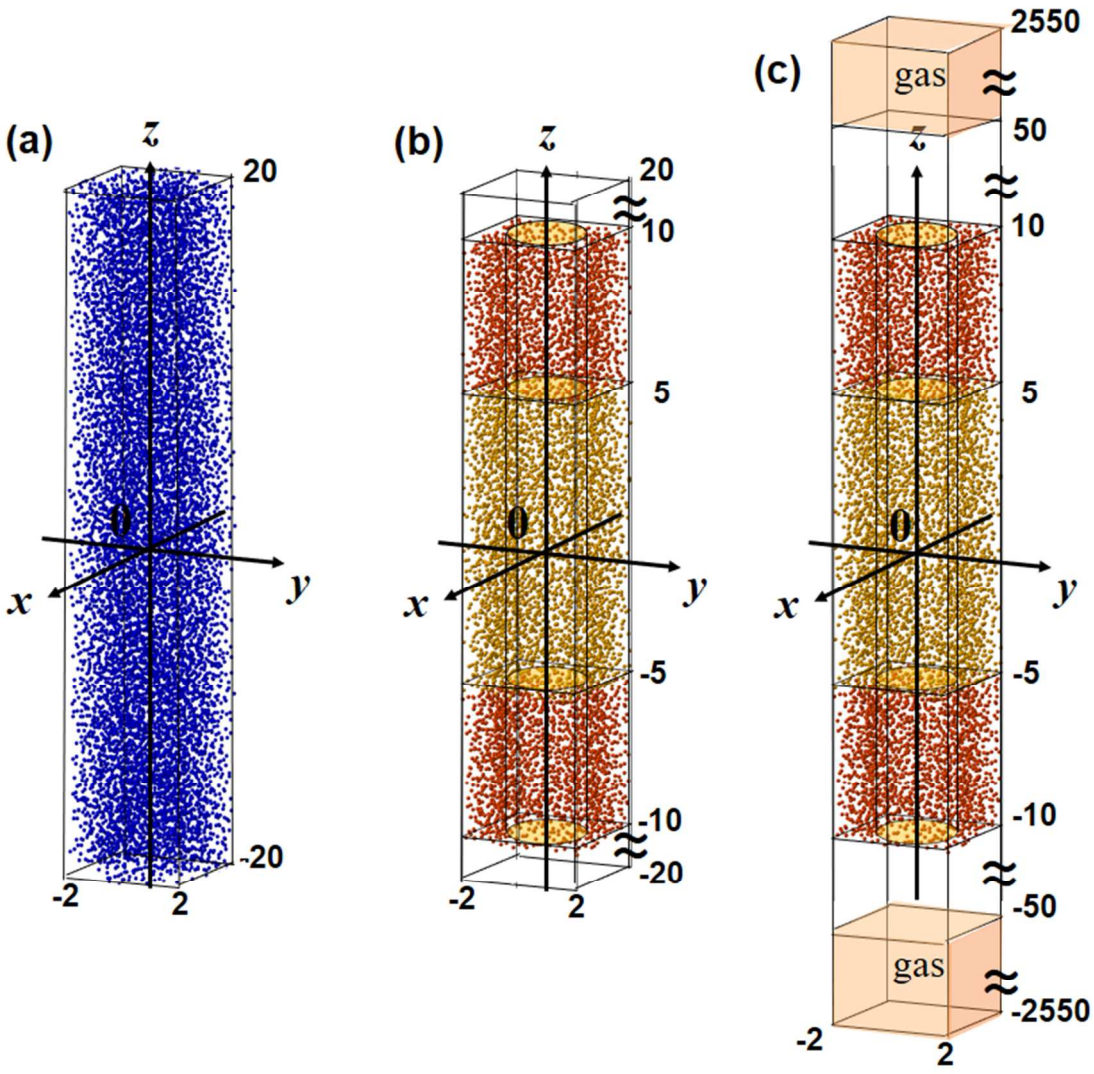

Fig. 1 Calculation systems for (a) bulk liquid, (b) adsorption-desorption isotherms and (c) adsorption and desorption processes. Blue dots are water molecules, whereas the red and yellow denote the outer and inner region molecules, respectively. All units are in nanometers and the figures are not to scale.

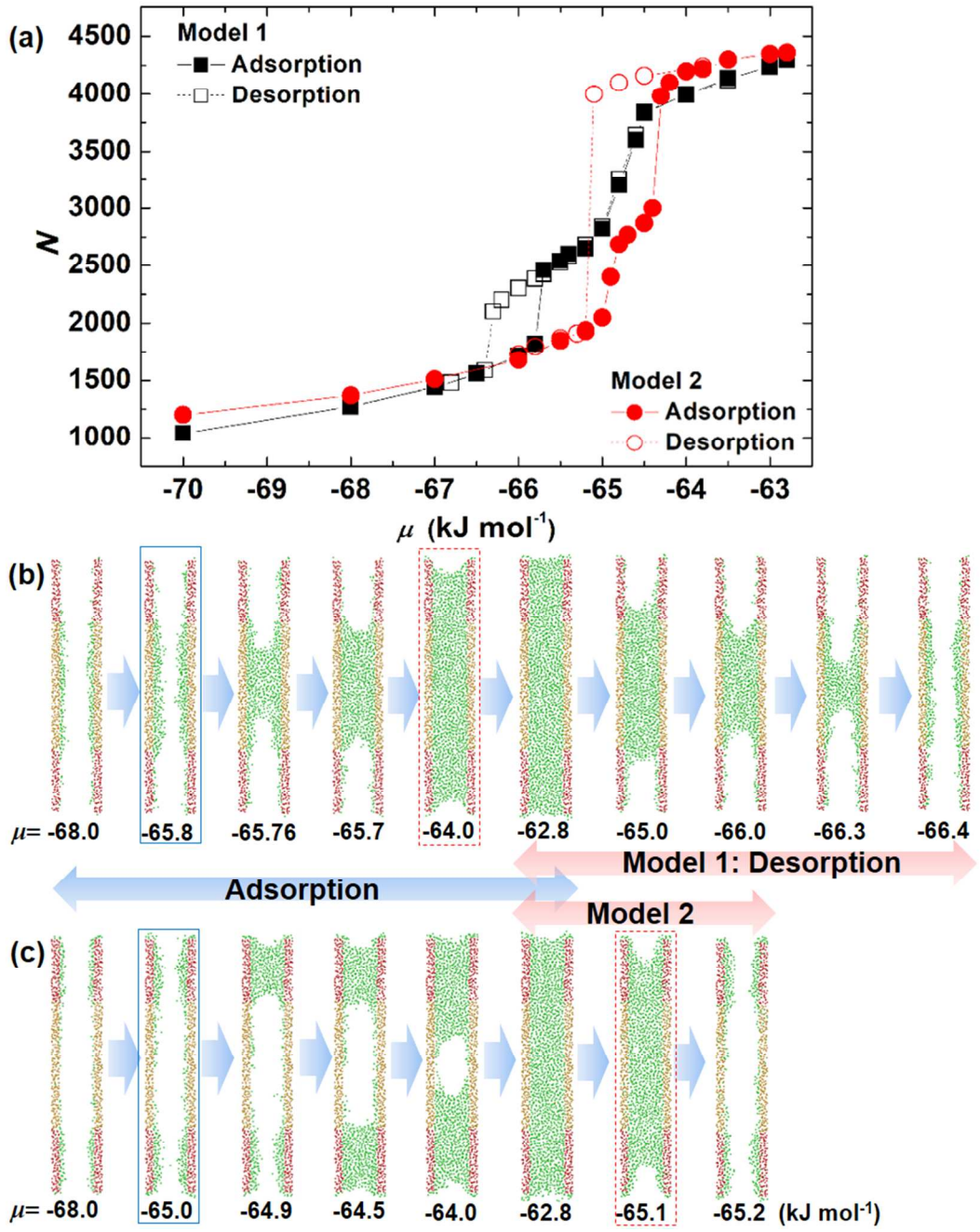

Fig. 2 (a) Adsorption-desorption isotherms for Model 1 and Model 2 from GCMC. The lines and arrows show the chemical potential differences used to produce the following cross-section snapshots during adsorption and desorption for (b) Model 1 and (c) Model 2. The boxed snapshots signify the initial chemical potential for adsorption or desorption.

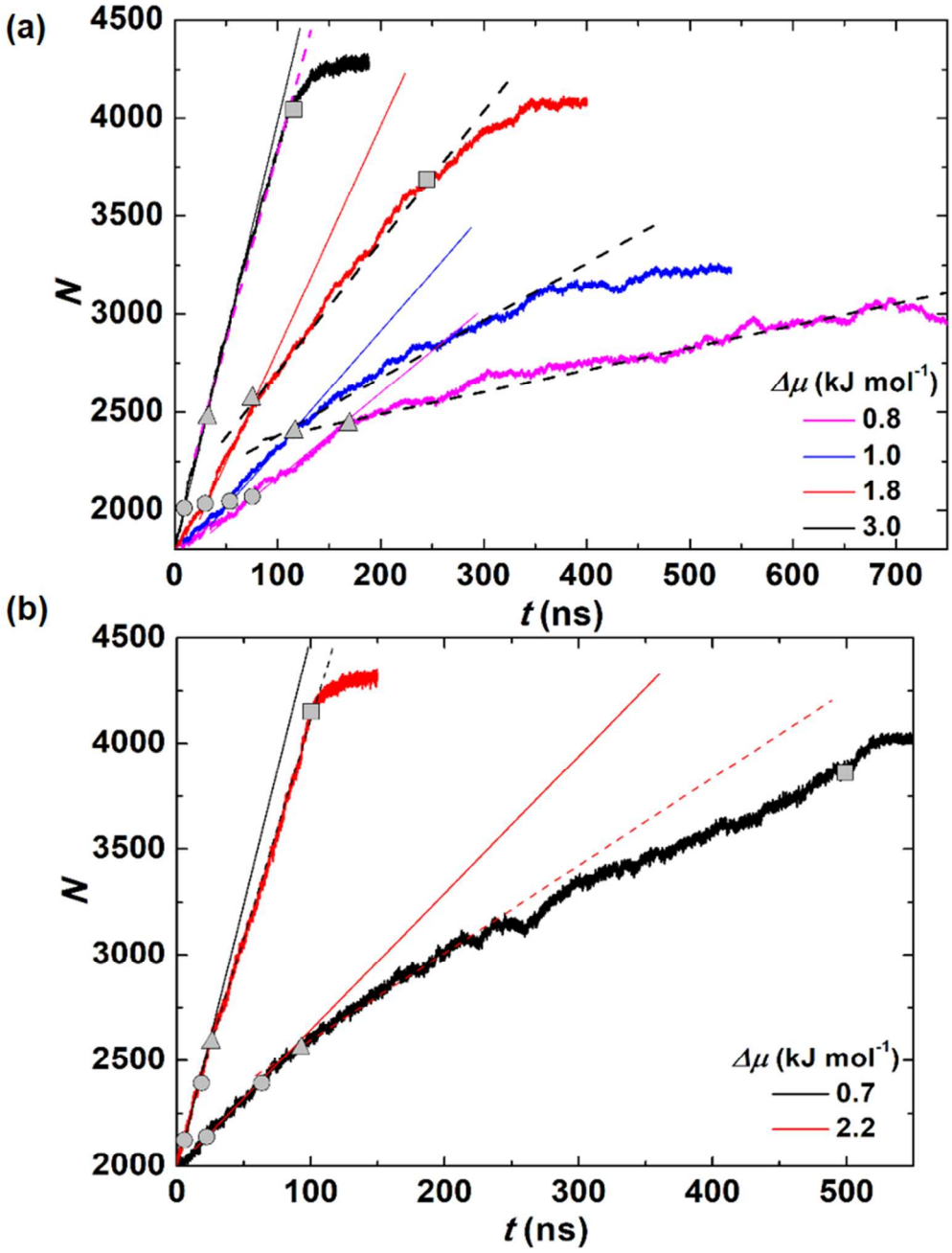

Fig. 3 (a) Filling rate curves for Model 1 for various $\Delta\mu$ values. The origins of the solid lines are from t_1 in Table 3 and the dashed lines start from t_2, which correspond to the circle and triangle, respectively. (b) Filling rate curves for Model 2 for different $\Delta\mu$ values. The origins of the solid lines are from $t_{1\text{-}1}$ in Table 4 and the dashed lines start from t_2, which correspond to the first circle and triangle, respectively.

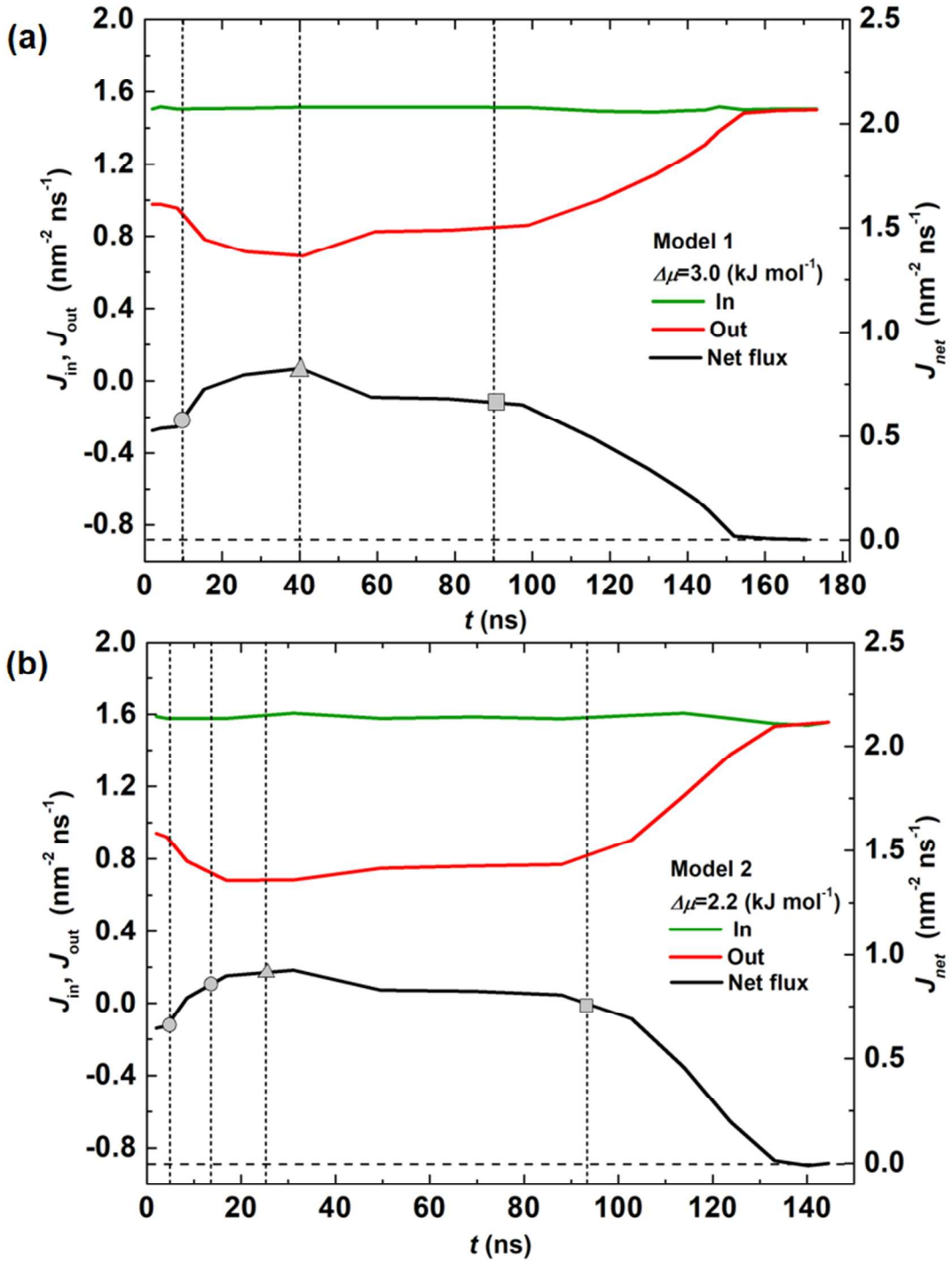

Fig. 4 Time evolution of flux sampled outside the pore at z= ±25 nm for (a) $\Delta\mu$ = 3.0 kJ mol^{-1} in Model 1, and (b) $\Delta\mu$ = 2.2 kJ mol^{-1} in Model 2. The shapes correspond to events explained in Fig 3.

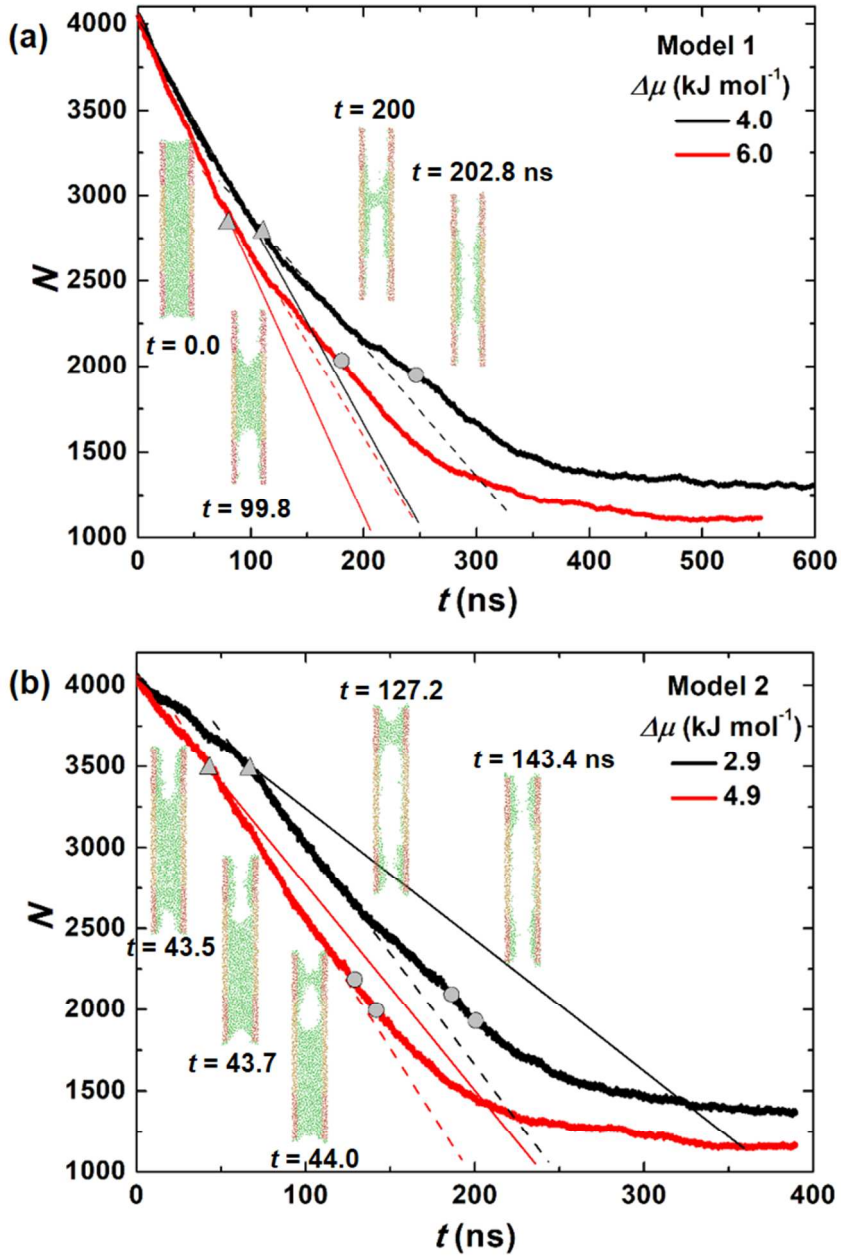

Fig. 5 (a) Desorption curves for Model 1 and corresponding snapshots of $\Delta\mu$ = 6.0 kJ mol^{-1}. (b) Desorption curves for Model 2 and corresponding snapshots of $\Delta\mu$ = 4.9 kJ mol^{-1}. The origins of the solid lines are from t=0 ns and the dashed lines start from the triangle, which corresponds to t_1 in Table 6. The fitted lines show the slope variation for different stages during the desorption process.

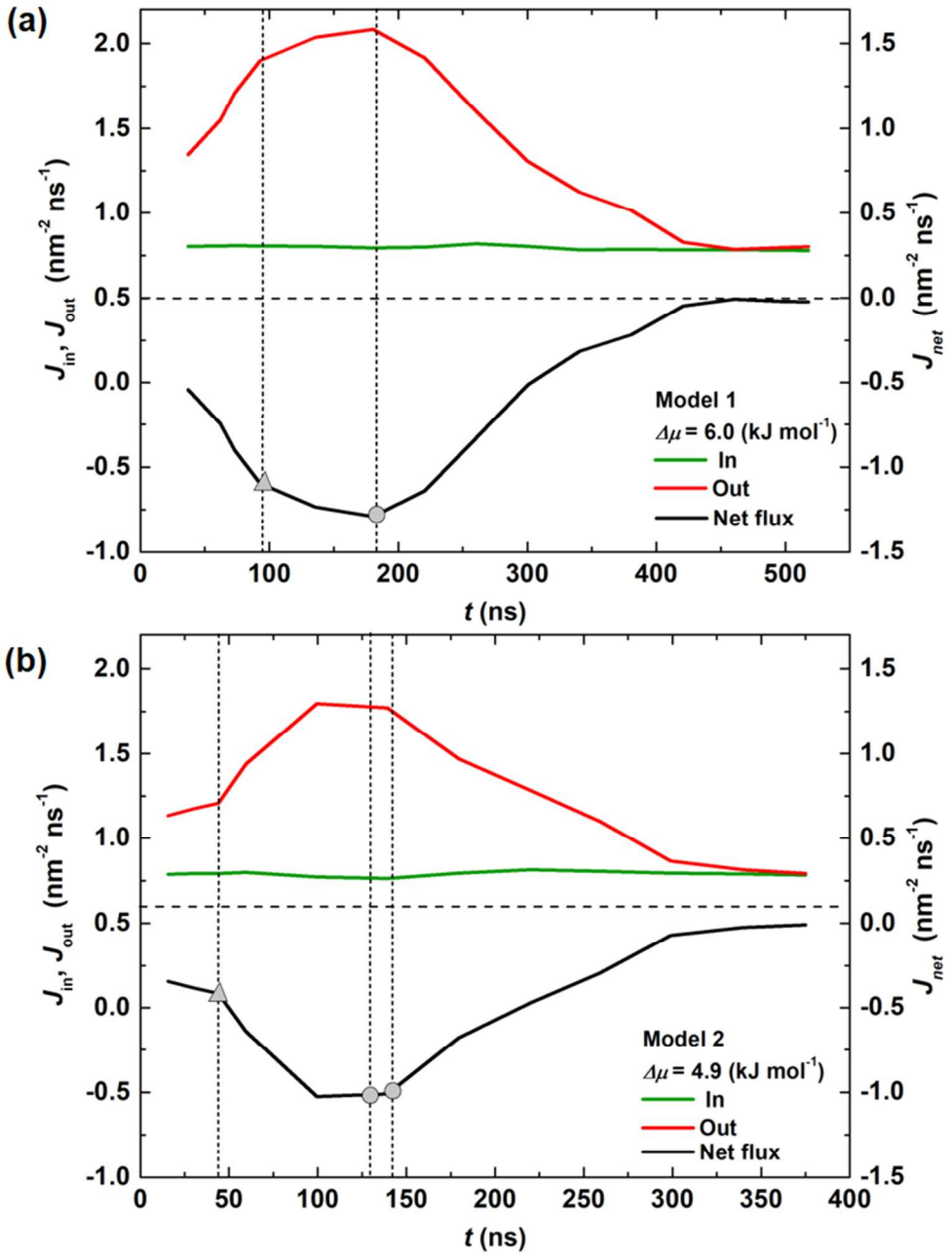

Fig. 6 Time evolution of the flux sampled outside the pore at z= ±25 nm for (a) $\Delta\mu$ = 6.0 kJ mol^{-1} in Model 1, and (b) $\Delta\mu$ = 4.9 kJ mol^{-1} in Model 2. The shapes correspond to events explained in Fig 5.

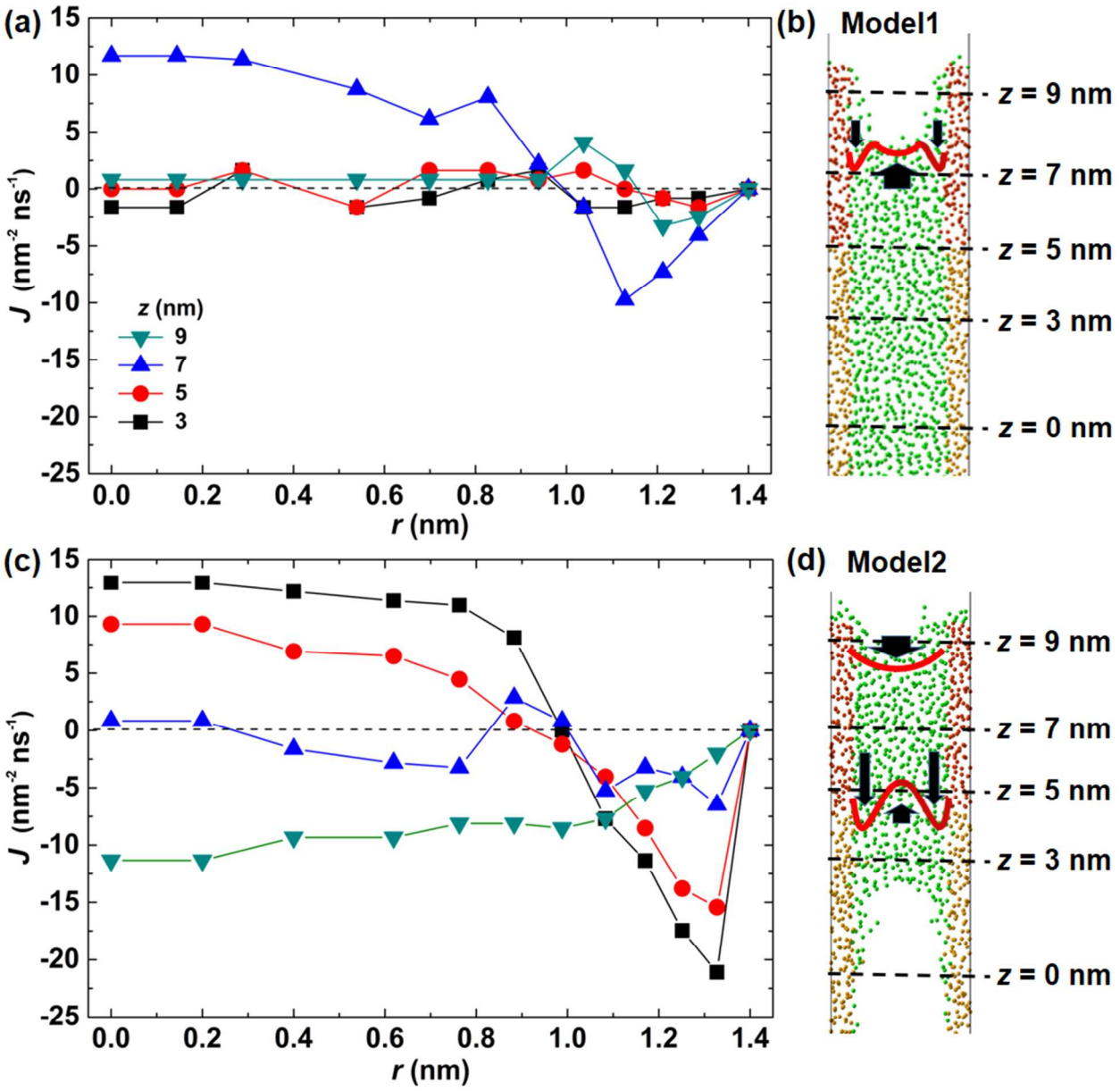

Fig. 7 Radial distribution of net flux during adsorption at different axial positions for (a) Model 1, $\Delta\mu$ = 3.0 kJ mol^{-1} at t= 85 ns and (b) corresponding snapshots and flow patterns at the menisci. (c) Model 2, $\Delta\mu$ = 2.2 kJ mol^{-1} at t= 65 ns and (d) corresponding snapshots and flow patterns at the menisci. The values are averaged since the system is axially symmetric.

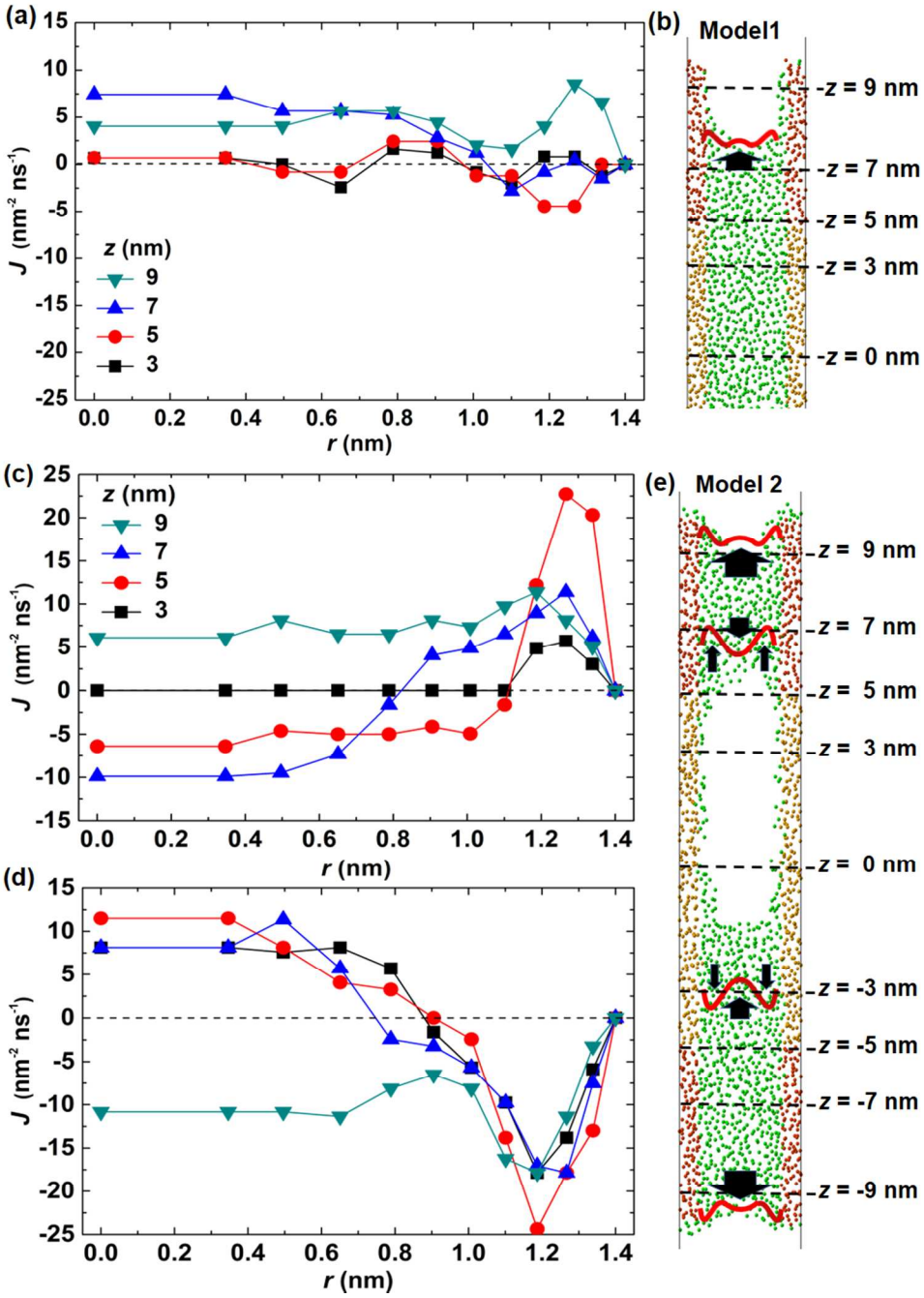

Fig. 8 Radial distribution of net flux during desorption at different axial positions for (a) Model 1, $\Delta\mu$ = 6.0 kJ mol^{-1} at t= 28 ns and (b) corresponding snapshot and flow patterns at the menisci. (c) Upper and (d) lower half of Model 2, $\Delta\mu$ = 4.9 kJ mol^{-1} at t= 60 ns and (e) corresponding snapshot and flow patterns around the menisci.

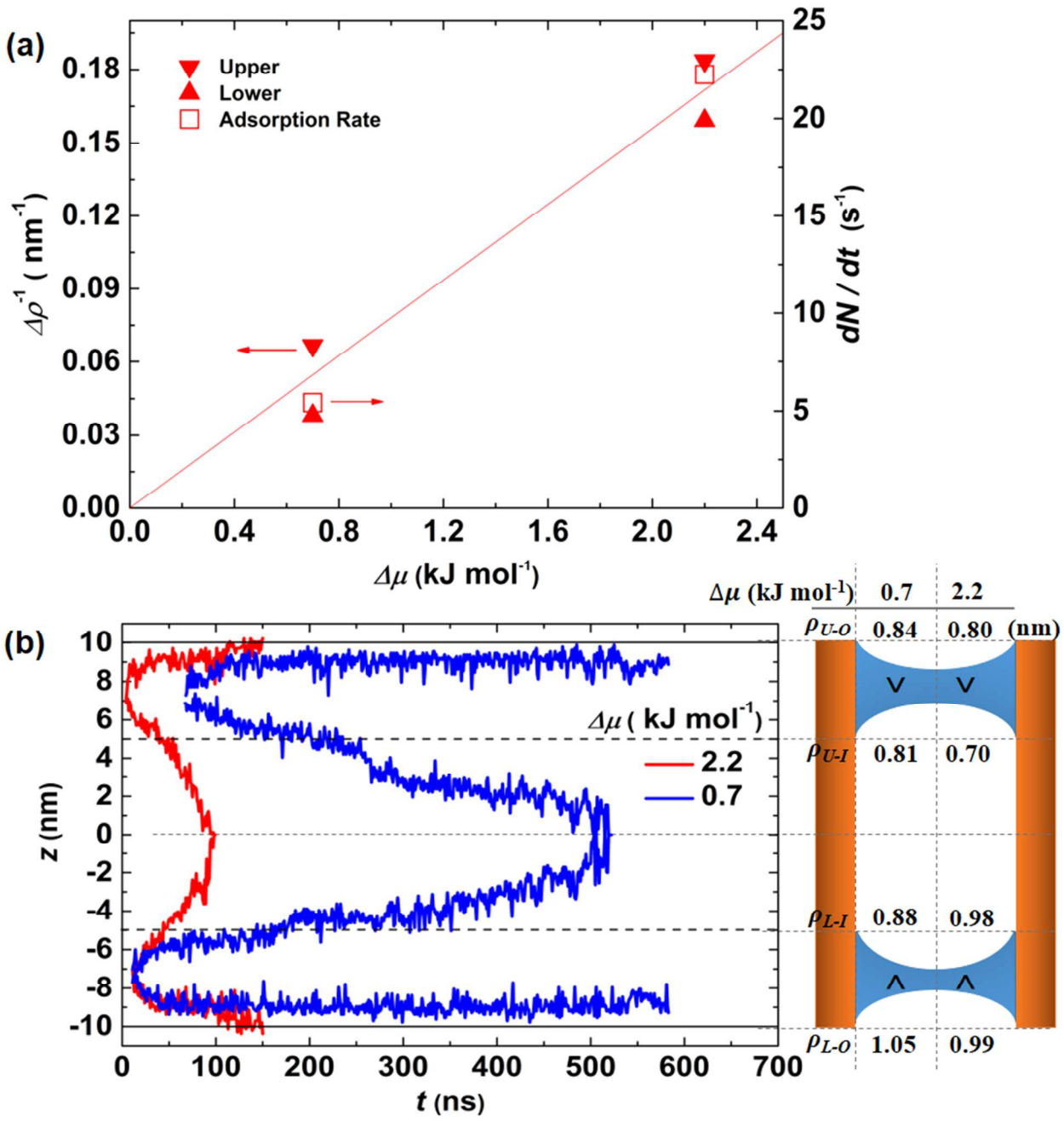

Fig. 9 (a) Averaged curvature difference of the menisci on both sides of the bridges in Model 2 at N = 2500 in Fig. 3 (b), and instantaneous adsorption rates (slopes) at N = 2500 for all $\Delta\mu$ conditions. (b) Evolution of menisci for all conditions and sketch of the radius of curvature for all conditions.

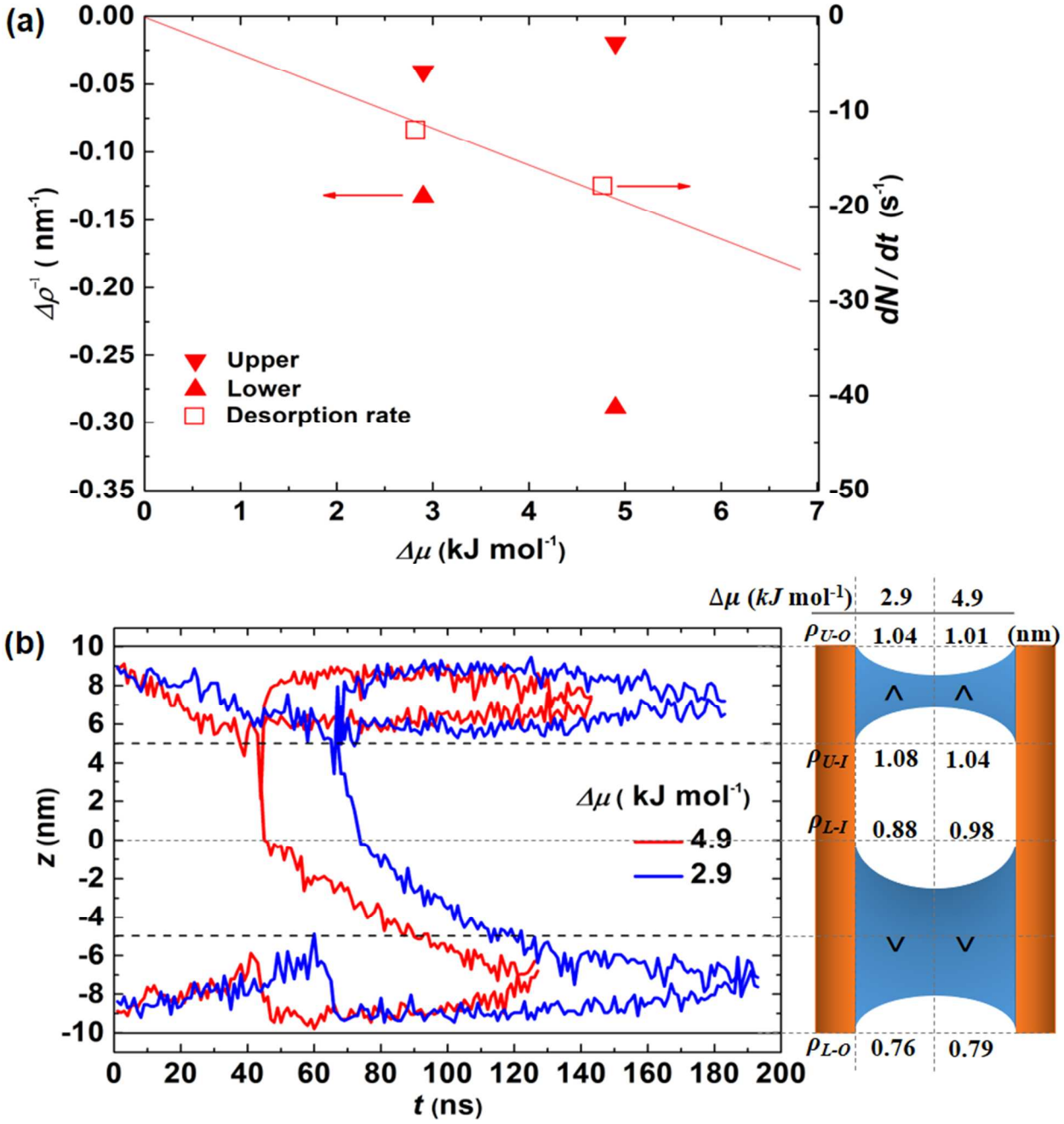

Fig. 10 (a) Averaged curvature difference of the menisci on both sides of the bridges in Model 2 at N = 3000 in Fig. 5 (b), and instantaneous desorption rates (slopes) at N = 3000 for all $\Delta\mu$ conditions. (b) Evolution of menisci for all conditions and sketch of the radius of curvature for all conditions.

Table 1. Parameters of the course-grained ELBA water model

	ELBA water		ELBA water
ε / kcal mol^{-1}	0.55	r_c / Å	12.0
σ / Å	3.05	m / g mol^{-1}	18.0
μ^I / D	2.6	I / g Å^2 mol^{-1}	30.0

Table 2. Parameters of water-wall atoms

	High hydrophilic	Low hydrophilic
$\varepsilon_{\text{water-wall}}$ / kJ mol^{-1}	0.80	0.50
μ^I_{wall} / D	4.0	2.0

Table 3. Summary of adsorption event times for Model 1

$\Delta\mu$ / kJ mol^{-1}	0.8	1.0	1.8	3.0
t_1 / ns	55	45	25	10
t_2 / ns	280	130	75	40
t_3 / ns	–	–	332	90

Table 4. Summary of adsorption event times for Model 2

$\Delta\mu$ / kJ mol^{-1}	0.7	2.2
$t_{1\text{-}1}$ / ns	18	5
$t_{1\text{-}2}$ / ns	70	14
t_2 / ns	90	25
t_3 / ns	480	93

Table 5. Summary of desorption event times for Model 1

$\Delta\mu$ / kJ mol^{-1}	4.0	6.0
t_1 / ns	105	80
t_2 / ns	260	193

Table 6. Summary of desorption event times for Model 2

$\Delta\mu$ / kJ mol^{-1}	2.9	4.9
t_1 / ns	65	44
$t_{2\text{-}1}$ / ns	184	127
$t_{2\text{-}2}$ / ns	194	143

TOC

The difference in adsorption and desorption characteristics depending on the hydrophilicity arrangements within a nanopore.